Determinants of target prioritization and regulatory hierarchy for the bacterial small RNA SgrS

Maksym Bobrovskyy[1,2] Jane K. Frandsen[3,4], Jichuan Zhang[5], Anustup Poddar[5], Muhammad S. Azam[1], Tina M. Henkin[3], Taekjip Ha[5,6] and Carin K. Vanderpool[1]*

[1]Department of Microbiology, University of Illinois at Urbana-Champaign, 601 S. Goodwin Ave., Urbana, Illinois 61801
[2]Present address: Department of Microbiology, The University of Chicago, 920 E. 58th St., Chicago, Illinois 60637
[3]Department of Microbiology and Center for RNA Biology, The Ohio State University, Columbus, Ohio 43210
[4]Biochemistry Program, The Ohio State University
[5]Department of Biophysics and Biophysical Chemistry, Johns Hopkins University, Baltimore, Maryland, USA 21205
[6]Howard Hughes Medical Institute, Baltimore, Maryland, USA 21205

*Corresponding author
Carin K. Vanderpool, Ph.D.
Department of Microbiology
University of Illinois at Urbana-Champaign
C213 CLSL, MC-110
601 S. Goodwin Ave.
Urbana, IL 61801
(t) 217-333-7033
(f) 217-244-6697
cvanderp@life.illinois.edu

Running title: Target prioritization by small RNAs

Abstract word count: 241

Text word count: 6,690

ABSTRACT

The mechanisms by which small RNA (sRNA) regulators select and prioritize target mRNAs remain poorly understood, but serve to promote efficient responses to environmental cues and stresses. We sought to uncover mechanisms that establish regulatory hierarchy for a model sRNA, SgrS, found in enteric bacteria and produced under conditions of metabolic stress when sugar transport and metabolism are unbalanced. SgrS post-transcriptionally controls a nine-gene regulon to restore growth and homeostasis under stress conditions. An *in vivo* reporter system was used to quantify SgrS-dependent regulation of target genes and established that SgrS exhibits a clear preference for certain targets, and regulates those targets efficiently even at low SgrS levels. Higher SgrS concentrations are required to regulate other targets. The position of targets in the regulatory hierarchy is not well-correlated with the predicted thermodynamic stability of SgrS-mRNA interactions or the SgrS-mRNA binding affinity as measured *in vitro*. Detailed analyses of SgrS interaction with *asd* mRNA demonstrate that SgrS binds cooperatively to two sites and remodels *asd* mRNA secondary structure. SgrS binding at both sites increases the efficiency of *asd* mRNA regulation compared to mutants that have only a single SgrS binding site. Our results suggest that sRNA selection of target mRNAs and regulatory hierarchy are influenced by several molecular features. The sRNA-mRNA interaction, including the number and position of sRNA binding sites on the mRNA and cofactors like the RNA chaperone Hfq, seem to tune the efficiency of regulation of specific mRNA targets.

58 **IMPORTANCE**

59 To survive, bacteria must respond rapidly to stress and simultaneously maintain
60 metabolic homeostasis. The small RNA (sRNA) SgrS mediates the response to stress
61 that arises from imbalanced sugar transport and metabolism. To coordinate the stress
62 response, SgrS regulates genes involved in sugar uptake and metabolism. Intrinsic
63 properties of sRNAs such as SgrS allow them to regulate extensive networks of genes.
64 To date, sRNA regulation of targets has largely been studied in the context of "one
65 sRNA-one target", and little is known about coordination of multi-gene regulons and
66 sRNA regulatory network structure. Here, we explore the molecular basis for regulatory
67 hierarchy in sRNA regulons. Our results reveal a complex interplay of factors, including
68 the number and location of sRNA binding sites on mRNA targets and the participation of
69 an RNA chaperone, that dictate prioritized regulation of targets to promote an efficient
70 response to stress.
71

72 **INTRODUCTION**

73 Bacteria live in diverse niches, often encountering rapidly changing and stressful
74 environments. Bacterial stress responses can mitigate the negative effects of stress on
75 cell structure and function. Stress responses are usually coordinated by molecules,
76 either RNAs or proteins, that alter expression of a regulon comprised of multiple genes.
77 Coordinated control of the regulon prepares the cell to survive or adapt to the stress (1).
78 Proteins control expression of target regulons by binding to DNA sequences and
79 modulating the frequency of transcription initiation, whereas RNAs often modulate gene
80 expression post-transcriptionally. A prevalent type of RNA regulator in bacteria is
81 referred to simply as small RNA (sRNA). The sRNAs are often produced in response to
82 a particular stress, and regulate target mRNAs through base pairing interactions that
83 modify mRNA translation or stability (2, 3). Hundreds of sRNAs have been identified in
84 diverse bacteria (4-6). While the majority of sRNAs have not been characterized, many
85 studies suggest that sRNA regulatory networks are as extensive and complex as those
86 controlled by proteins (7, 8).

87 A large body of work has illuminated base pairing-dependent molecular
88 mechanisms of post-transcriptional regulation by sRNAs (9, 10). The sRNA SgrS
89 (sugar-phosphate stress sRNA) has been an important model for discovery of both
90 negative and positive mechanisms of target mRNA regulation. SgrS is induced in
91 response to metabolic stress associated with disruption of glycolytic flux and
92 intracellular accumulation of sugar phosphates (also referred to as glucose-phosphate
93 stress) (11, 12). SgrS regulates at least 9 genes and promotes recovery from glucose-
94 phosphate stress. SgrS-dependent repression of mRNAs encoding sugar transporters

95 (*ptsG, manXYZ*) reduces uptake of sugars to prevent further sugar-phosphate
96 accumulation (Fig. 1) (11, 13, 14). Activation of a sugar phosphatase (*yigL*) mRNA
97 promotes dephosphorylation and efflux of accumulated sugars (15), and repression of
98 other mRNAs is hypothesized to reroute metabolism to promote recovery from stress
99 (Fig. 1) (16). Each target of SgrS is regulated by a distinct molecular mechanism. How
100 different mechanisms of regulation yield effects of variable magnitude with respect to
101 mRNA stability and translation is an open question.

102 Temporally-ordered and hierarchical patterns of gene regulation carried out by
103 protein transcription factors have been characterized in many systems (17-20). These
104 regulatory patterns allow cells to respond efficiently to environmental signals by
105 prioritizing induction or repression of products needed to respond to those signals.
106 Protein regulators establish a hierarchy of regulation based on their affinities for binding
107 sites in the operator regions of different target genes. As the concentration of active
108 regulator increases, genes are sequentially regulated based on binding site affinity (21).
109 There is growing evidence that sRNAs also regulate their target genes hierarchically
110 (22, 23). However, the mechanisms involved in establishing and maintaining prioritized
111 regulation of sRNA targets are not known.

112 We hypothesize that the temporal progression of target regulation by SgrS is
113 optimized to promote efficient recovery from glucose-phosphate stress (Fig. 1). To test
114 this hypothesis, we first defined the efficiency of SgrS regulation of each target and
115 found that SgrS indeed prioritizes regulation of some targets over others. We examined
116 the factors that determine regulatory efficiency, including the arrangement and strength
117 of SgrS target binding sites and the roles of other factors like RNase E and Hfq.

118 Detailed characterization of a specific SgrS-mRNA target interaction revealed
119 cooperative binding of SgrS to two binding sites and a requirement for both binding sites
120 for maximal SgrS-dependent regulation. Collectively, our results uphold the hypothesis
121 that sRNAs regulate expression of genes in their target regulons hierarchically, and that
122 this is influenced by features of each sRNA-mRNA pair and different molecular
123 mechanisms of regulation that precisely determine the regulatory priority for each target.

124 **RESULTS**

125 **SgrS differentially regulates targets at the level of translation.** Previous studies
126 suggested the possibility of a regulatory hierarchy for the small RNA SgrS, which
127 regulates a diverse set of mRNA targets (10, 11, 13-15). To study this, we used a two-
128 plasmid system to control expression of SgrS and target translational fusions (Fig. 2A).
129 All target transcript fragments fused to *gfp* contain experimentally-confirmed SgrS
130 binding sites. To quantify translational regulation by SgrS and facilitate comparisons of
131 regulatory efficiency among targets, we analyzed the data as described previously (23).
132 Activity of reporter fusions was measured by monitoring GFP fluorescence over time. By
133 plotting the GFP fluorescence (RFU) as a function of growth (OD_{600}) for target-*gfp*
134 fusions in the absence of SgrS, we defined "basal activity" at different inducer
135 concentrations (example in Fig. S1A). This method of quantifying fusion activity
136 accounts for the fact that fluorescence levels are not directly proportional to inducer
137 concentrations ((23) and Fig. S1A). While the absolute values for basal activity differ
138 among different fusions, all fusions responded to induction in a dose-dependent manner
139 (Fig. S2A). Similar plots (RFU/OD_{600}) were generated for each fusion in the presence of
140 SgrS (examples Fig. S1B-F). We define "regulated activity" as the slope of the curve

141 (RFU/OD_{600}) under conditions where both the fusion and SgrS are induced (example in
142 Fig. S1B). As levels of SgrS increase, clear patterns of repression or induction are seen
143 for all target fusions (Figs S1B-F and S2B-F).

144 To define the efficiency of regulation of each target, we plotted regulated activity
145 as a function of basal activity for *ptsG*, *manX, asdI, purR,* and *yigL*. When there is no
146 SgrS-mediated regulation, a line with a slope of 1 is seen for all targets (Fig. 2B-F).
147 Slopes less than 1 indicate that the fusion is repressed by SgrS. This is true for *ptsG*,
148 *manX*, *asdI* and *purR* reporter fusions (Figure 2B-E). Slopes greater than 1 are
149 indicative of activation by SgrS, as seen for *yigL* (Fig. 2F). The magnitude of regulation
150 was responsive to SgrS levels over the range of SgrS inducer (aTc) concentrations (Fig.
151 2B-E). In contrast, for for *yigL,* the magnitude of activation did not increase beyond a
152 maximal level obtained at 20 ng/mL of inducer (Fig. 2F). While the basis for this
153 difference is unclear, it is likely to reflect the inherently different molecular mechanisms
154 of regulation, *i.e.,* mRNA stabilization for *yigL* and translational repression for other
155 targets.

156 We then compared regulatory efficiency of targets at different levels of SgrS
157 induction. At the two lowest levels of SgrS induction (10ng/mL and 20 ng/mL aTc), only
158 *ptsG* and *yigL* showed substantial repression and activation, respectively (Fig. 3A, B). In
159 contrast, *manX*, *asdI* and *purR* fusions yielded curves whose slopes remained at ~1,
160 indicating no regulation at lower levels of SgrS. Our interpretation is that *ptsG* and *yigL*
161 are high-priority targets of SgrS, since they are regulated preferentially when SgrS
162 levels are low. With increasing SgrS levels (20-50 ng/ml aTc), regulation of “weaker”
163 targets *manX, asdI* and *purR* became apparent (Fig. 3C, D, E). As SgrS levels

164 increased, *ptsG* repression became more efficient up to a maximal repression at 40
165 ng/mL of aTc, and it remained the most strongly repressed target at all levels of SgrS.
166 Collectively, these data suggest that SgrS targets are preferentially regulated in the
167 following order: 1/2) *ptsG* and *yigL*, 3) *manX,* 4) *asdI*, and 5) *purR* (Fig. 3A-E). We
168 hypothesize that the position of each target within the regulatory hierarchy is determined
169 by characteristics of SgrS-target mRNA interactions and the mechanism of SgrS-
170 dependent regulation.

171 **Differences in binding affinity *in vitro* are not correlated with regulation efficiency.**
172 One of the initial steps in sRNA-mediated regulation is formation of base-pairing
173 interactions with the target mRNA. Binding of the sRNA with its target mRNA is
174 dependent on sequence complementarity and RNA secondary structure. We examined
175 the characteristics of SgrS-target mRNA binding *in vitro* to determine whether the
176 strength of binding is correlated with the target hierarchy.

177 Electrophoretic mobility shift assays (EMSAs) were performed to measure
178 binding of SgrS to its target mRNAs *ptsG*, *manX*, *purR*, *yigL* and *asd*. SgrS bound to
179 *ptsG* with a K_D of 0.11 ± 0.01 μM (Fig. 4A, B), which was lower than K_Ds for SgrS
180 binding to most of the other targets (Fig. 4A-E). SgrS-*manX* mRNA binding had a K_D of
181 19.7 ± 2.78 μM (Fig. 4A, C), which is weaker than the interaction with *ptsG* (Fig. 4B), but
182 stronger compared to *purR* and *yigL* (Fig. 4A). Three different fragments of *asd* mRNA
183 were tested, because previous work demonstrated that SgrS pairs at two distinct sites
184 on *asd* mRNA (16). The first site, *asdI*, is adjacent to the ribosome binding site and is
185 sufficient for modest SgrS-dependent translational repression. The second site, *asdII,* is
186 in the coding sequence of *asd,* 60-nt downstream of the start codon. When both sites

187 are present (RNA *asdI-II*), stronger SgrS-dependent translational repression was
188 observed (16). Surprisingly, while *asdI* RNA (containing only the upstream SgrS binding
189 site) regulation was less efficient compared to that of *manX* (Fig. 3A-E), *in vitro* it bound
190 SgrS more strongly with a K_D of 0.15 ± 0.04 μM (Fig. 4A, D), which is comparable to
191 SgrS-*ptsG* binding (Fig. 4A, B). SgrS interaction with *asdII* was very weak (Fig. 4A). We
192 could not determine K_D values for SgrS interaction with *asdII*, *purR* and *yigL*, due to
193 limitations in obtaining high enough concentrations of RNA, but it is apparent that SgrS
194 binding to these targets is much weaker compared to *ptsG*, *manX* and *asdI* (Fig. 4A).
195 Results of EMSAs with SgrS and *asdI-II* (containing both SgrS binding sites)
196 revealed apparent binding cooperativity. SgrS binding to *asdI-II* has a K_D of 0.07 ± 0.01
197 μM (Fig. 4E, F), slightly lower than that of SgrS-*ptsG* mRNA binding. Moreover, we
198 observed two shifted species that correspond to binding of either one or two SgrS
199 sRNAs to a single *asdI-II* RNA (Fig. 4E).
200 **Structural analyses of SgrS-*asd* mRNA interactions.** Our data thus far indicate that
201 SgrS regulates mRNA targets in a hierarchical fashion (Figs. 2, 3). However, SgrS-
202 mRNA binding affinities do not explain the target hierarchy, as SgrS-*ptsG* mRNA and
203 SgrS-*asd* mRNA interactions have very similar K_Ds, but *ptsG* is much more efficiently
204 regulated than *asd* at all concentrations of SgrS (Fig. 3). To further understand the
205 features that influence the efficiency of target regulation, we performed more detailed
206 analyses of SgrS-*asd* mRNA interactions.
207 Previous work demonstrated that SgrS binding site I encompasses nt +31 to +49
208 and site II encompasses nt +110 to +127 ((16), Fig. 5A). We used IntaRNA (24, 25) to
209 predict the free energy (ΔG) for SgrS interactions with *asd* mRNA segments containing

210 both sites, or each site individually (Fig. 5B). IntaRNA accounts for the energy of
211 opening double-stranded RNA secondary structure, to make sequences accessible for
212 pairing. We first analyzed SgrS interactions with *asdI-II* mRNA (nt +1 to +240), which we
213 denote as "structured." Interaction of SgrS with *asd* site I has a predicted ΔG of -10.5
214 kcal/mol, while SgrS pairing with site II has a predicted ΔG of -1.1 kcal/mol (Fig. 5B,
215 structured). The ΔG for interactions between SgrS and the isolated binding sites are -18
216 kcal/mol for site I and -7.4 kcal/mol for site II (Fig. 5B, isolated). These predictions
217 suggest that SgrS interaction with site II is less favorable, particularly in the context of
218 the longer structured *asd* mRNA.

219 We investigated the structure of *asdI-II* with selective 2'-hydroxyl acylation
220 analyzed by primer extension (SHAPE), in which flexible nts are modified by N-
221 methylisotoic anhydride (NMIA), while nts constrained in helices are not reactive. In the
222 absence of SgrS, the sequence encompassing the *asd* ribosome binding site (+44 to
223 +50) is located within a structured loop (+36 to +69) on top of a short stem (+31 to +35
224 pairing with +70 to +74) (Fig. 5C, Fig. S3). The nts in site I (+31 to +49, Fig. 5A) are
225 located on the 5' side of the stem-loop structure. Most of the nts in this structure are
226 reactive, which is indicative of a flexible conformation that is accessible for ribosome
227 binding or base pairing with the seed sequence of SgrS (Fig. 5C). The seed interaction
228 of SgrS is likely to promote opening of the structure. Downstream of the site I stem-loop
229 structure is a highly structured second stem (+83 to +155) that contains site II in the
230 apical region (+110 to +129) (Fig. 5C, Fig. S3). Site II is sequestered in a helix and
231 would not be accessible to base pair with SgrS (Fig. 5C). In light of binding cooperativity

232 observed in Fig. 4E, we hypothesize that SgrS pairing with site I induces rearrangement
233 of *asd* mRNA secondary structure to facilitate interaction with site II.
234 We next used SHAPE to probe changes in the *asdI-II* structure in the presence of
235 SgrS. The reactivity of site I nt +31 to +49 decreased as the concentration of SgrS
236 increased (Fig. 5D), with the exception of nt +41 which is not predicted to base pair with
237 SgrS (Fig. 5A). The SHAPE reactivity plateaued between 5- and 10-fold excess SgrS
238 (Fig. S3E,F), which suggests that binding to site I was saturated. This is consistent with
239 a strong base-paring interaction between SgrS and site I. In contrast, the reactivity of
240 the site II nts +110 to +129 decreased more slowly and to a lesser extent (Fig. 5D),
241 consistent with a weaker and cooperative interaction. Fewer site II nts showed changes
242 in SHAPE reactivity upon addition of SgrS; this is likely to be due to the highly
243 structured nature of site II in the absence of SgrS.
244 The reactivity of nts outside of the SgrS binding sites also changed in the
245 presence of SgrS (Fig. 5E). In contrast, when a mutant SgrS that is not predicted to bind
246 to *asdI-II* was used, minimal changes in SHAPE reactivity were observed, which
247 suggests that the changes in the presence of wild-type SgrS are due to the specific
248 interactions between SgrS and *asdI-II* mRNA and not to the presence of additional RNA
249 in the system (Fig. 5E). These results indicate that SgrS binding changes the overall
250 structure of the *asd* RNA. A secondary structure predicted using the SHAPE data
251 suggests that these changes are limited to opening the SgrS binding sites and
252 extending the site II stem (Fig. 5C). We note an important caveat to these analyses. The
253 structure prediction algorithms were not designed to account for intermolecular
254 interactions, so this analysis may not be able to capture the *in vivo* relevant structure of

255 *asd* mRNA in complex with SgrS. Nonetheless, SHAPE data are consistent with other
256 analyses in demonstrating binding of SgrS to *asd* mRNA, prominently at site I and to a
257 lesser extent at site II.

258 **Optimal repression by SgrS involves both pairing sites within *asd* mRNA.** To
259 further investigate the role of the two SgrS pairing sites on *asd*, we performed stochastic
260 optical reconstruction microscopy (STORM) coupled with single-molecule *in situ*
261 hybridization (smFISH) to monitor SgrS regulation of *asd-lacZ* variants *asdI, asdII,* and
262 *asdI-II* (Fig. 6A) at single molecule resolution. In these experiments, bacteria were
263 grown in the presence of L-arabinose to induce expression of chromosomal *asd-lacZ*
264 variants, and glucose-phosphate stress was induced for 10 min by the addition of 1% α-
265 methyl D-glucopyranoside (αMG). 3D super-resolution images show *asd-lacZ* mRNAs
266 (Fig. 6B-D, green) and SgrS (Fig. 6B-D, red), as projected on 2D planes, with cells
267 outlined. Numbers of *asd-lacZ* mRNAs and SgrS sRNAs were counted and represented
268 as "copy number per cell" in histograms, with average copy number per cell indicated
269 above the histogram (Fig. 6B-D). SgrS induction reduced the copy number of *asdI-lacZ*
270 RNA by 3-fold (Fig. 6B, green) when SgrS was induced to high levels after 10 min
271 treatment with αMG (Fig. 6B, red and S4A, B). In contrast, the copy number of *asdII-*
272 *lacZ* RNAs (Fig. 6C, green) was not strongly affected in the presence of high SgrS
273 levels after αMG treatment (Fig. 6C, red and Fig. S4C, D). Copy numbers of *asdI-II-lacZ*
274 RNA (Fig. 6D, green) were reduced by ~8-fold after 10 min of αMG induction (Fig. 6D,
275 red, Fig. S6E,F). These data demonstrate that both binding sites on *asd* mRNA are
276 important for efficient SgrS-dependent regulation of mRNA stability.

277 We next examined the roles of the two SgrS binding sites in the efficiency of
278 translational regulation. SgrS regulation of an *asdI-II* translational fusion was compared
279 to regulation of an *asdI* fusion (Fig. 7A). By plotting regulated activity as a function of
280 basal activity as described above, we determined that SgrS repression of *asdI-II* was
281 more efficient than repression of *asdI* across a range of SgrS expression levels (Fig.
282 7B), a result in line with our previous study (16). Comparison to other targets indicated
283 that *asdI-II* is regulated more efficiently than *manX*, *asdI* and *purR*, at all concentrations
284 of SgrS (Fig. 7C).

285 We then compared SgrS regulation of *asdI* and *asdI-II* in the *rne701* mutant
286 strain deficient in degradosome assembly (26). We determined basal activity (Fig. S5A)
287 and regulated activity (Fig. S5B-F) of *asdI* and *asdI-II* translational *gfp* fusions at
288 different levels of SgrS induction. Similar to our data for the wild-type strain (Fig. 7A),
289 SgrS regulated *asdI-II* more efficiently compared to *asdI* in the *rne701* mutant (Fig. 7D).
290 Moreover, when compared to SgrS regulation of other targets, *asdI-II* was repressed
291 most efficiently (Fig. 7E) in the *rne701* mutant. Taken together the data indicate that the
292 second binding site on *asd* mRNA enhances the stringency of SgrS-mediated
293 regulation. Moreover, addition of the second binding site on *asd* changes its regulatory
294 priority relative to other targets in the SgrS regulon.

295 **Transcriptional regulation of *asd* by SgrS.** We observed that the *asdI-II* RNA is more
296 abundant than *asdI* (Fig. 6B, D). Since the constructs used in that experiment were
297 expressed from a heterologous promoter, we postulated that increased levels of *asdI-II*
298 compared to *asdI* mRNA must be due to increased mRNA stability or transcription
299 elongation of the *asdI-II* construct compared to *asdI.* We therefore constructed *asdI* and

300 *asdI-II* transcriptional fusions to *lacZ* expressed from an inducible promoter (Fig. 8A) to
301 test whether SgrS can regulate *asd* transcripts independent of translational regulation.
302 Consistent with observations from smFISH, the *asdI-II-lacZ* transcriptional fusion had
303 substantially higher activity compared to *asdI-lacZ* (Fig. 8B). Repression of *asdI-II* by
304 SgrS was more efficient (3.3-fold repression) than was observed for *asdI* (2.1-fold
305 repression) (Fig. 8B). SgrS still regulated both fusions in the *rne701* mutant strain (Fig.
306 8B). Importantly, SgrS-dependent degradation of other SgrS targets (*ptsG* mRNA (27)
307 and *manXYZ* mRNA (13, 14)) was abolished in degradosome mutants. Together with
308 our previous work, these observations suggest that SgrS regulates *asd* by two
309 independent mechanisms, translational repression by pairing at site I (directly occluding
310 the ribosome binding site) and reducing mRNA levels by promoting mRNA turnover
311 and/or inhibiting transcription elongation.

312 **DISCUSSION**

313 In this study, we set out to define the hierarchy of regulation by a model bacterial
314 sRNA. SgrS is a good model for this study because it has a modestly-sized regulon,
315 and the mechanisms of regulation of several targets have been characterized in detail
316 (13, 15, 16, 28). Our results demonstrate a clear pattern of prioritized regulation of
317 mRNA targets (Fig. 2B-F, Fig. 3A-E). Two targets in particular, *ptsG* and *yigL,* were
318 "high-priority" targets that were efficiently regulated even at low levels of SgrS. Other
319 targets, *manX, purR,* and *asd,* were less impacted by SgrS and were regulated only
320 when SgrS was produced at higher levels.

321 We investigated features of sRNA-mRNA interactions that could impact the
322 overall efficiency of SgrS-mediated regulation. SgrS-mRNA interactions *in vitro*, as

323 measured by EMSA defined K_Ds, were not well-correlated with *in vivo* regulatory
324 efficiency (Fig. 4A-F, Fig. 3A-E). Two targets stood out in the comparison of *in vivo*
325 regulation and *in vitro* SgrS-mRNA interactions. The *yigL* mRNA interaction with SgrS
326 was barely detectable *in vitro* (Fig. 4A), but *in vivo*, *yigL* translation was maximally
327 activated at low SgrS levels (Fig. 2F). Conversely, the translation of *asdI* was modestly
328 regulated by SgrS *in vivo* (Fig. 2E), but the *in vitro* SgrS-*asdI* interaction was
329 comparable to that of SgrS-*ptsG*, which had the strongest *in vivo* regulatory effect.
330 These apparent contradictions between *in vitro* interactions and *in vivo* regulatory
331 efficiency led us to further explore SgrS regulation of *asd.*
332 Previous work demonstrated that SgrS has two binding sites on *asd* mRNA: site I
333 overlaps that *asd* ribosome binding site and site II is ~60 nt downstream in the *asd*
334 coding sequence ((16) and Fig. 5A). EMSAs demonstrated SgrS pairing at site I alone,
335 but pairing at site II alone was undetectable. Binding of SgrS to an *asd* mRNA
336 containing both sites I and II was cooperative (Fig. 4E,F). Structural analyses of *asd*
337 mRNA in the absence and presence of SgrS demonstrated that SgrS indeed pairs
338 preferentially at site I over site II and induces substantial structural rearrangement in the
339 mRNA (Fig. 5C-E, Fig. S3). Quantification of SgrS-dependent degradation of *asd* mRNA
340 showed that site I is important, but sites I and II together promote the most efficient
341 regulation (Fig. 6B-D, Fig. S4). Similar to binding and regulation of mRNA degradation,
342 SgrS interactions at both sites I and II on *asd* mRNA improve the efficiency of
343 translational regulation (Fig. 7B,C, Fig. S2). These results suggest that the number and
344 position of sRNA binding sites on mRNA targets control regulation *in vivo* in ways that
345 could not be predicted based on *in vitro* characterization of sRNA-mRNA binding.

346 In many cases, sRNA-mediated regulation of translation is thought to indirectly
347 affect mRNA stability by making untranslated mRNA more susceptible to degradation by
348 RNase E. There are also examples of sRNA regulation, including SgrS regulation of
349 *yigL* (15), where modulation of mRNA stability is translation-independent. Truncation of
350 RNase E (encoded by *rne*), removing the C-terminal scaffold for degradosome
351 assembly, often prevents sRNA-mediated degradation of mRNA targets (14, 29, 30). If
352 translational regulation is the primary function of an sRNA on a given mRNA target, the
353 regulation should be preserved in *rne* mutant backgrounds. For SgrS targets, the
354 regulatory hierarchy is mostly preserved in an *rne701* degradosome mutant background
355 (Fig. 7, compare C and E), suggesting that for most targets, regulation of RNA stability
356 is not the primary mechanism of control by SgrS. Interestingly, the high-priority target
357 *ptsG* was a notable exception. In the wild-type background, *ptsG* is the most efficiently-
358 regulated target (Fig. 7C), whereas in the *rne701* host, it is weakly regulated. This
359 defect could be overcome by increasing SgrS expression levels (Fig. S6B). This result
360 suggests that RNase E-dependent degradation of *ptsG* mRNA is more important for its
361 efficient regulation by SgrS compared to other targets, where efficient regulation does
362 not depend on subsequent target degradation. This is consistent with the fact that *ptsG*
363 mRNA levels decrease at least 10-fold whereas other targets exhibit a modest 2-fold
364 decrease in mRNA levels upon SgrS expression (16). Our recent study quantifying
365 SgrS-dependent mRNA degradation at single molecule resolution indicated that *ptsG*
366 mRNA exhibits faster degradation kinetics than *manXYZ* mRNA (29), which could
367 enhance the efficiency of regulation in a wild-type but not *rne701* mutant background
368 where translational regulation and mRNA degradation are uncoupled.

369 One of our ultimate goals is to define at a molecular level the mechanisms by
370 which sRNAs select and prioritize regulation of their targets. The current study
371 implicates features of sRNA-mRNA interactions such as number and strength of sRNA
372 binding sites on each mRNA target and accessory factors such as RNase E in dictating
373 regulatory hierarchy. Another factor that is likely to play an important role in setting
374 regulatory priority is the RNA chaperone Hfq. EMSAs demonstrated Hfq binding to
375 *ptsG*, *manX*, *purR*, *yigL*, *asdI*, *asdII* and *asdI-II* mRNAs (Fig. S7A) with similar K_D values
376 for all targets (Fig. S7B). Previous work has shown that sRNAs compete for binding to
377 Hfq, and this competition affects their regulatory ability (31, 32). Different sRNAs can
378 bind to distinct sites on Hfq and this impacts their regulation of particular targets (32,
379 33). Additional work will be required to determine what role Hfq plays in establishing the
380 hierarchy of regulatory effects in sRNA regulons.
381 Most sRNA-mRNA interactions are conceived of as single binding site
382 interactions, but we have already identified two SgrS targets that deviate from this
383 model and have shown that additional binding sites can play important roles in
384 regulation and change regulation efficiency (13, 16). We have not yet discovered the
385 specific mechanism of regulation of *asd* mRNA by SgrS, but have shown definitively
386 that both binding sites are required for strong regulation. SgrS-dependent control of
387 both transcriptional and translational *asd* reporter fusions is not impacted in RNase E
388 degradosome deficient strains (Fig. 7B,D, Fig. 8B), suggesting that the regulation is not
389 strictly dependent on translation or mRNA turnover. Future work will test the hypothesis
390 that SgrS acts on *asd* mRNA at the level of transcription elongation, perhaps by an
391 attenuation mechanism.

392 In *Vibrio*, quorum sensing-regulated Qrr sRNAs regulate multiple targets by
393 distinct mechanisms and differences in those mechanisms influence the dynamics and
394 strength of regulation (22). Strong and rapid regulation is achieved by sRNAs acting
395 catalytically, whereby the sRNA pairs with and promotes mRNA degradation but is then
396 recycled for use on another mRNA target. A sequestration mechanism, where formation
397 of the sRNA-mRNA complex is the terminal outcome of regulation, results in slower and
398 weaker sRNA-dependent regulation of the target mRNA. For Qrr sRNAs, these
399 regulatory mechanisms seem to depend on which region of the sRNA is pairing with a
400 given target and whether the sRNA-mRNA interaction is strong or weak (22). While
401 some of the same features of SgrS-mRNA interactions may be relevant in determining
402 regulatory efficiency, we note that the SgrS seed sequence responsible for pairing with
403 all mRNA targets characterized thus far is encompassed by a short (~20 nt) mostly
404 single-stranded region of SgrS (11, 14-16). Moreover, we did not see a good correlation
405 between strong versus weak binding *in vitro* and *in vivo* regulatory efficiency. It is
406 possible that the “rules” governing regulatory efficiency and specific outcomes are
407 different for each individual sRNA. Detailed analysis of more model sRNAs will be
408 needed to illuminate broad general principles.
409 Beyond defining interesting molecular features of sRNA-mRNA interactions,
410 defining regulatory hierarchy for sRNA regulons is important for understanding bacterial
411 physiology. The vast majority of sRNA regulons remain undefined, and thus many
412 sRNA functions are unknown. For novel sRNAs, distinguishing high-priority from weaker
413 targets may provide crucial clues to the predominant role of the sRNA in cell physiology.
414 For SgrS, the regulatory hierarchy we have defined here is perfectly consistent with

415 growth studies that demonstrate the primary importance of SgrS regulation of sugar
416 transport and efflux under glucose-phosphate stress conditions (34). The hierarchy of
417 regulation by sRNAs is likely to have evolved to promote rapid and efficient responses
418 to environmental signals that would provide cells with a competitive growth advantage in
419 their specific niche. It will be crucial to develop tools to more rapidly characterize sRNA
420 regulatory hierarchy to better understand the functions of the hundreds of
421 uncharacterized sRNAs in diverse bacteria.

422 **MATERIALS AND METHODS**

423 **Strain and plasmid construction.** Strains and plasmids used in this study are listed in
424 Table S1. All strains used in this study are derivatives of *E. coli* K-12 strain MG1655.
425 Oligonucleotide primers and 5' biotinylated probes used in this study are listed in Table
426 S2 and were purchased from Integrated DNA Technologies. Chromosomal alleles were
427 moved between strains by P1 *vir* transduction (35) and inserted using λ Red
428 recombination (36, 37).

429 Translational reporter fusion alleles P_{BAD}-*asdI-II-lacZ* (MBP151F/MBP193R
430 primers), P_{BAD}-*asdI-lacZ* (MBP151F/MBP151R primers) and P_{BAD}-*asdII-lacZ*
431 (MBP193F/MBP193R primers) were constructed by PCR amplification of desired
432 fragments using primers containing homologies to P_{BAD} and *lacZ.* Similarly,
433 transcriptional fusions P_{BAD}-*asdI-II-lacZ* (MBP151F/MBP206R3 primers) and P_{BAD}-*asdI-*
434 *lacZ* (MBP151F/MBP206R1 primers) were generated by PCR amplification using a
435 forward primer with homology to P_{BAD} and reverse primers containing *lacZ* RBS and
436 *lacZ* homology. PCR products were then recombined into PM1205 strain using λ Red
437 homologous recombination.

438 A plasmid harboring SgrS under the control of P_{tet0-1} promoter was constructed
439 by PCR amplification of *sgrS* from *E. coli* MG1655 chromosomal DNA using primers
440 containing NdeI and BamHI restriction sites. The resulting PCR product and vector
441 pZA31R (23) were digested with NdeI and BamHI (New England Biolabs) restriction
442 endonucleases. Digestion products were ligated using DNA Ligase (New England
443 Biolabs) to produce plasmid pZAMB1 containing P_{tet0-1}-*sgrS* allele.
444 Plasmid pZEMB8 containing P_{lac0-1}-*ptsG-gfp* was constructed by PCR
445 amplification of *ptsG* from MG1655 chromosomal DNA using primers containing KpnI
446 and EcoRI restriction sites. The resulting PCR products and vector pZE12S (23) were
447 digested with KpnI and EcoRI restriction endonucleases. Digestion products were
448 ligated using DNA Ligase to produce pZEMB2. Superfolder *gfp* (referred to as *gfp*) was
449 amplified from pXG10-SF (38) using primrs containing KpnI and XbaI restriction sites.
450 pZEMB2 and the resulting PCR product were digested with KpnI and XbaI, and ligated
451 with DNA ligase to produce pZEMB8. Plasmids with translational reporter fusions P_{lac0-1}-
452 *manX-gfp* (pZEMB10), P_{lac0-1}-*yigL-gfp* (pZEMB15), P_{lac0-1}-*purR-gfp* (pZEMB25), P_{lac0-1}-
453 *asdI-gfp* (pZEMB26) and P_{lac0-1}-*asdI-II-gfp* (pZEMB27) were constructed by restriction
454 cloning into pZEMB8 using KpnI and EcoRI restriction endonucleases.
455 **Media and reagents.** Bacteria were cultured in Luria-Bertani (LB) broth medium or LB
456 agar plates (35) at 37°C, unless stated otherwise. Bacteria were grown in MOPS
457 (morpholine-propanesulfonic acid) rich defined medium (Teknova) with 0.2% fructose
458 for reporter fluorescence assays. When necessary, media were supplemented with
459 antibiotics at the following concentrations: 100 μg/ml ampicillin (Amp), 25 μg/ml
460 chloramphenicol (Cm), 25 μg/ml kanamycin (Kan) and 50 μg/ml spectinomycin (Spec).

461 Isopropyl β-D-1-thiogalactopyranoside (IPTG) was used at concentrations of 0.1-1.5
462 mM for induction of P_{lac0-1} promoter, anhydrotetracycline (aTc) was used at 0-50 ng/ml
463 for induction of P_{tet0-1} promoter and L-arabinose was used at 0.000002%-0.2% for
464 induction of P_{BAD} promoter, unless otherwise noted. To induce glucose-phosphate
465 stress, 0.5% α-methylglucoside (αMG) was added to the growth medium.
466 **Reporter fluorescence assay.** Bacterial strains were cultured overnight in MOPS rich
467 medium supplemented with 0.2% fructose, Amp, and Cm, and diluted 1:100 into fresh
468 medium with appropriate inducers (IPTG, aTc) in 48 well plates. Relative fluorescence
469 units (RFU) and optical density (OD_{600}) were measured over time. "GFP expression"
470 was calculated by plotting RFU over OD_{600} and determining the slopes of linear
471 regression plots for each IPTG concentration in exponentially growing cells in the
472 presence of aTc to induce SgrS expression. "Promoter activity" was calculated by
473 plotting RFU over OD_{600} and determining the slopes of linear regression plots for each
474 IPTG concentration in exponentially growing cells in the absence of aTc.
475 ***In vitro* transcription and radiolabeling***.* Template DNA for *in vitro* transcription was
476 generated by PCR using gene-specific oligonucleotides containing the T7 RNA
477 polymerase promoter sequence. The following oligonucleotides were used to generate
478 specific template DNA: MBP84F/MBP213R–*ptsG* (+1 to +240), O-JH218/MBP214R–
479 *manX* (+1 to +240), MBP56F/MBP215R–*asdI-II* (+1 to +240), MBP56F/MBP222R–*asdI*
480 (+1 to +110), MBP226F/MBP226R–*asdII* (+71 to +310), MBP65F/MBP174R–*purR* (+1
481 to +230), MBP216F/MBP216R–*yigL* (-191 to +50 relative to ATG translation start of
482 *yigL*) MBP234F/MBP234R–*gfp* (+1 to +240) and O-JH219/O-JH119 were used to
483 generate full-length *sgrS* template DNA. *In vitro* transcription of DNA templates was

484 performed according to specifications of the MEGAscript T7 Kit (Ambion). *In vitro*
485 transcribed RNA was 5'-end labeled with radioisotope ^{32}P using the KinaseMax Kit
486 (Ambion), according to the manufecturer's instructions. Samples were purified by
487 passing through Illustra ProbeQuant G-50 Micro Columns (GE Healthcare) followed by
488 extraction with phenol-chloroform:isoamyl alcohol (Ambion), and labeled RNA was
489 precipitated with ethanol:3M NaAc (30:1).
490 **RNA-RNA gel electrophoretic mobility shift assay**. Different concentrations of
491 unlabeled mRNA were mixed with 0.02 pmol of 5'-end labeled SgrS. Samples were
492 denatured at 95°C for 1 min, placed on ice for 5 min, and incubated at 37°C for 30 min
493 in 1x binding buffer (20 mM Tris-HCL [pH 8.0], 1mM DTT, 1 mM $MgCl_2$, 20 mM KCl, 10
494 mM Na_2HPO_4 [pH 8.0]) (39). Non-denaturing loading buffer was added and samples
495 were resolved for 6 h at 40 V on native 5.6% PAGE.
496 **Protein-RNA gel electrophoretic mobility shift assay.** 0.02 pmol of 5'-end labeled
497 mRNA was denatured at 95°C for 1 min, and placed on ice for 5 min. Different
498 concentrations of purified Hfq protein (His-tagged) were added. Samples were
499 incubated at 37°C for 30 min in 1x binding buffer. Non-denaturing loading buffer was
500 added and samples were resolved for 90 min at 20 mA on native 4.0% PAGE (39).
501 **SHAPE.** The *asdI-II* RNA (0.15 μM) and SgrS RNA (0.075 μM, 0.15 μM, 0.30 μM, 0.75
502 μM, 1.5 μM, or 3.0 μM) were folded separately as in (40) using a modified SHAPE
503 buffer (100 mM HEPES [pH 8.0], 2 mM $MgCl_2$, 40 mM NaCl). For each SgrS
504 concentration, the SgrS RNA or the equivalent volume of 0.5X TE was added to the
505 *asdI-II* RNA and the samples were incubated at 37°C for 30 min. The RNAs were
506 modified with *N*-methylisatoic anhydride (NMIA, 6.5 mM; Sigma-Aldrich) and collected

507 by ethanol precipitation as in (40). Parallel primer extension inhibition and sequencing
508 reactions were performed using fluorescently labeled primers complementary to the 3'
509 end of the *asdI-II* RNA (5′-AGATCAAAGGCATCCTGAAG, 22.5 nM; Applied
510 Biosystems, ThermoFisher Scientific) as in (41) with minor modifications. Prior to primer
511 binding, the RNAs were denatured and snap cooled and the reactions were carried out
512 for 20 min at 52˚C, followed by 5 min at 65˚C. The cDNAs were analyzed on a 3730
513 DNA Analyzer (Applied Biosystems, Inc.). The data were processed and SHAPE
514 reactivity (difference between the frequency of primer extension products at each
515 nucleotide in +NMIA vs. -NMIA samples) was derived using the QuShape software (42).
516 Data for each nucleotide were averaged with statistical outliers removed and normalized
517 using the 2-8% rule (43). Relative reactivity was calculated by subtracting normalized
518 SHAPE reactivity in the absence of the SgrS RNA from reactivity in the presence of the
519 WT or MT SgrS RNA.
520 **Single-molecule fluorescence *in situ* hybridization (smFISH).** The *asdI-lacZ*
521 (MB170), *asdII-lacZ* (MB183) and *asdI-II-lacZ* (MB171) strains were grown overnight at
522 37ºC with shaking at 250 rpm in LB Broth Miller (EMD) containing Kan and Spec. The
523 next day, the overnight cultures were diluted 100-fold into MOPS EZ rich defined
524 medium (Teknova) with 0.2% (w/w) sodium succinate, 0.02% glycerol and L-arabinose
525 (0.01% for the *asdI-lacZ* and *asdII-lacZ* strains, 0.002% for *asdI-II-lacZ*) and were
526 allowed to grow at 37ºC till the OD_{600} reached 0.15-0.25. αMG was added to the culture
527 to a desired concentration to introduce sugar phosphate stress and induce SgrS sRNA
528 expression. After 10 min of induction, the cells were fixed by mixing with formaldehyde
529 (Fisher Scientific) at a final concentration of 4%.

530 Δ*sgrS* and Δ*lacZ* strains were grown in LB Broth Miller (EMD) at 37ºC with
531 shaking at 250 rpm overnight. The cultures were diluted 100-fold into MOPS EZ rich
532 defined medium (Teknova) with 0.2% glucose and allowed to grow at 37ºC until the
533 OD_{600} reached 0.2. The cells were then fixed by mixing with formaldehyde at a final
534 concentration of 4%. TK310 cells were grown overnight, similar to the knockout strains.
535 The overnight culture was then diluted 100-fold into MOPS EZ rich defined medium
536 (Teknova) with 0.2% glucose and 1 mM isopropyl β-D-1-thiogalactopyranoside (IPTG,
537 Sigma-Aldrich) and allowed to grow at 37ºC for 30 minutes. The cells were then fixed as
538 described above.
539 The fixation and permeabilization of the cells were done using the methods
540 published previously (44). After fixing with 4% formaldehyde, the cells were incubated at
541 room temperature for 30 min. The cells were then centrifuged at 600 x g for 7 min and
542 the pellets were washed with three times with 1X PBS 3. The cells were then
543 permeabilized with 70% ethanol for 1 h at room temperature and stored at 4ºC before
544 fluorescence *in situ* hybridization.
545 The smFISH probes were designed using Stellaris Probe Designer and
546 purchased from Biosearch Technologies (https://www.biosearchtech.com/). The labeling
547 of the probes was performed using equal volumes of each probe. The final volume of
548 sodium bicarbonate was adjusted to 0.1 M by adding 1/9 reaction volume of 1 M sodium
549 bicarbonate (pH = 8.5). The probe solution was mixed with 0.05-0.25 mg of Alexa Fluor
550 647 or Alexa Fluor 568 succinimidyl ester (Life Technologies) dissolved in 5 μL DMSO.
551 The dye was kept at 20-25 fold in molar excess relative to the probes. After incubation
552 with gentle vortexing in the dark at 37ºC overnight, the reaction was quenched by

553 adding 1/9 reaction volume of 3 M sodium acetate (pH 5). Unconjugated dye was
554 removed by ethanol precipitation followed by P-6 Micro Bio-Spin Column (Bio-Rad).
555 A previously published protocol (44) was used for the hybridization procedure. 60
556 µl of permeabilized cells were washed with FISH wash solution (10% formamide in 2X
557 SSC [Saline Sodium Citrate] buffer) and resuspended in 15 µl hybridization buffer (10%
558 dextran sulfate, 1 mg/ml *E. coli* tRNA, 0.2 mg/ml BSA, 2 mM vanadyl ribonucleoside
559 complexes, 10% formamide in 2X SSC) with probes. Nine probes labeled with Alexa
560 Fluor 647 were used for sRNA SgrS and 24 probes labeled with Alexa Fluor 568 were
561 used for mRNA *lacZ*. The concentration of the labeled probes for SgrS and *lacZ* mRNA
562 were 50 nM and 15 nM, respectively. The reactions were incubated in the dark at 3 ºC
563 overnight. The cells were then resuspended in 20X volume FISH wash solution and
564 centrifuged. They were then resuspended in FISH wash solution, incubated for 30 min
565 at 30ºC and centrifuged and this was repeated 3 times. The cells were pelleted after the
566 final washing step and resuspended in 20 µl 4X SSC and stored at 4ºC for imaging. The
567 labeled cells were immobilized on a poly-L-lysine (Sigma-Aldrich) treated 1.0
568 borosilicate chambered coverglass (Thermo Scientific™ Nunc™ Lab-Tek™). They were
569 then imaged in imaging buffer (50 mM Tris-HCl [pH = 8.0], 10% glucose, 1% β-
570 mercaptoethanol [Sigma-Aldrich], 0.5 mg/ml glucose oxidase [Sigma-Aldrich] and 0.2%
571 catalase [Calbiochem] in 2X SSC).
572 **Single-molecule localization-based super-resolution imaging.** An Olympus IX-71
573 inverted microscope with a 100X NA 1.4 SaPo oil immersion objective was used for the
574 3D super-resolution imaging. The lasers used for two-color imaging were Sapphire 568-
575 100 CW CDRH, Coherent (568nm) and DL640-100-AL-O, Crystalaser (647nm) and

576 DL405-025. Crystalaser (405nm) was used for the reactivation of Alexa 647 and Alexa
577 568 fluorophores. The laser excitation was controlled using mechanical shutters
578 (LS6T2, Uniblitz). A dichroic mirror (Di01-R405/488/561/635, Semrock) was used to
579 reflect the laser lines to the objective. The objective collected the emission signals and
580 then they made their way through an emission filter (FF01-594/730-25, Semrock for
581 Alexa 647 or HQ585/70M 63061, Chroma for Alexa 568) and excitation laser was
582 cleaned up using notch filters (ZET647NF, Chroma, NF01-568/647-25x5.0 and NF01-
583 568U-25, Semrock). Samples were then imaged on a 512x512 Andor EMCCD camera
584 (DV887ECS-BV, Andor Tech). Astigmatism was introduced by placing a cylindrical lens
585 with a focal length of 2 m (SCX-50.8-1000.0-UV-SLMF-520-820, CVI Melles Griot) in
586 the emission path between two relay lenses with focal lengths of 100 mm and 150 mm
587 each, which facilitated 3D imaging. In this setup, each pixel corresponded to 100 nm.
588 We used the CRISP (Continuous Reflective Interface Sample Placement) system (ASI)
589 to keep the z-drift of the setup to a minimum. The image acquisition was controlled
590 using the storm-control software written in Python by Zhuang and coworkers (45, 46)
591 and available at GitHub.
592 The imaging of the sample began with a DIC image of the sample area.
593 Subsequently two-color super-resolution imaging was performed. 647nm excitation was
594 used first and after image acquisition was completed for Alexa Fluor 647, 568nm
595 excitation was used to image Alexa Fluor 568. 405 nm laser power was increased
596 slowly to compensate for fluorophore bleaching and also to maintain moderate signal
597 density. Imaging was stopped when most of the fluorophores had photobleached and
598 the highest reactivation laser power was reached.

599 The raw data acquired using the acquisition software were analyzed using the
600 method described in previously published work (29), which was a modification of the
601 algorithm published by Zhuang and coworkers (45, 46). The clustering analysis on the
602 localization data was performed using MATLAB codes as described previously (29).
603 Background signal was estimated using Δ*sgrS* and Δ*lacZ* strains and they were
604 prepared, imaged and analyzed as described above. TK310 cells were prepared,
605 imaged and analyzed in the same way as a low copy *lacZ* mRNA sample for copy
606 number calculation. The copy number calculation was also performed using MATLAB
607 codes as described previously (29).

608 **ACKNOWLEDGEMENTS**

609 We would like to extend a special thank you to Erel Levine for providing
610 plasmids. We are grateful to Jennifer Rice, Rich Yemm, Divya Balasubramanian,
611 Chelsea Lloyd, Alisa King, Jessica Kelliher and other current and past members of the
612 Vanderpool lab for strains, plasmids and valuable advice. We appreciate and thank
613 Prof. James Slauch and members of his lab for fruitful discussions.

614 **FUNDING**

615 National Institutes of Health R01 GM092830 (M.B. and C.K.V.), R01 GM112659 (M.B.,
616 M.S.A., T.H., J.Z., and A.P.), R35 GM122569 (T.H., J.Z., and A.P.), R01 GM047823
617 (T.M.H.), T32 GM086252 (J.K.F.); National Science Foundation PHY 1430124 (T.H.,
618 J.Z., and A.P); University of Illinois Department of Microbiology James R. Beck
619 Fellowship (M.B.).

620

621 **REFERENCES**

622 1. Fang FC, Frawley ER, Tapscott T, Vazquez-Torres A. 2016. Bacterial stress responses
623 during host infection. Cell Host Microbe 20:133-43.
624 2. Georg J, Hess W. 2011. *Cis*-antisense RNA, another level of gene regulation in bacteria.
625 Microbiology and molecular biology reviews : MMBR 75:286-300.
626 3. Storz G, Vogel J, Wassarman KM. 2011. Regulation by small RNAs in bacteria:
627 expanding frontiers. Mol Cell 43:880-91.
628 4. Carroll RK, Weiss A, Broach WH, Wiemels RE, Mogen AB, Rice KC, Shaw LN. 2016.
629 Genome-wide annotation, identification, and global transcriptomic analysis of regulatory
630 or Small RNA Gene Expression in Staphylococcus aureus. MBio 7:e01990-15.
631 5. Koo JT, Lathem WW. 2012. Global discovery of small noncoding RNAs in pathogenic
632 *Yersinia* species. Adv Exp Med Biol 954:305-14.
633 6. Zhang A, Wassarman KM, Rosenow C, Tjaden BC, Storz G, Gottesman S. 2003. Global
634 analysis of small RNA and mRNA targets of Hfq. Mol Microbiol 50:1111-24.
635 7. Salvail H, Masse E. 2012. Regulating iron storage and metabolism with RNA: an
636 overview of posttranscriptional controls of intracellular iron homeostasis. Wiley
637 Interdiscip Rev RNA 3:26-36.
638 8. Sharma CM, Papenfort K, Pernitzsch SR, Mollenkopf HJ, Hinton JC, Vogel J. 2011.
639 Pervasive post-transcriptional control of genes involved in amino acid metabolism by the
640 Hfq-dependent GcvB small RNA. Mol Microbiol 81:1144-65.
641 9. Bobrovskyy M, Vanderpool CK. 2013. Regulation of bacterial metabolism by small RNAs
642 using diverse mechanisms. Annu Rev Genet 47:209-32.
643 10. Bobrovskyy M, Vanderpool CK, Richards GR. 2015. Small RNAs regulate primary and
644 secondary metabolism in gram-negative bacteria. Microbiol Spectr 3.
645 11. Vanderpool CK, Gottesman S. 2004. Involvement of a novel transcriptional activator and
646 small RNA in post-transcriptional regulation of the glucose phosphoenolpyruvate
647 phosphotransferase system. Mol Microbiol 54:1076-89.
648 12. Vanderpool CK, Gottesman S. 2007. The novel transcription factor SgrR coordinates the
649 response to glucose-phosphate stress. J Bacteriol 189:2238-48.
650 13. Rice JB, Balasubramanian D, Vanderpool CK. 2012. Small RNA binding-site multiplicity
651 involved in translational regulation of a polycistronic mRNA. Proc Natl Acad Sci U S A
652 109:E2691-8.
653 14. Rice JB, Vanderpool CK. 2011. The small RNA SgrS controls sugar-phosphate
654 accumulation by regulating multiple PTS genes. Nucleic Acids Res 39:3806-19.
655 15. Papenfort K, Sun Y, Miyakoshi M, Vanderpool CK, Vogel J. 2013. Small RNA-mediated
656 activation of sugar phosphatase mRNA regulates glucose homeostasis. Cell 153:426-37.
657 16. Bobrovskyy M, Vanderpool CK. 2016. Diverse mechanisms of post-transcriptional
658 repression by the small RNA regulator of glucose-phosphate stress. Mol Microbiol
659 99:254-73.
660 17. Chevance FF, Hughes KT. 2008. Coordinating assembly of a bacterial macromolecular
661 machine. Nat Rev Microbiol 6:455-65.
662 18. Syed KA, Beyhan S, Correa N, Queen J, Liu J, Peng F, Satchell KJ, Yildiz F, Klose KE.
663 2009. The *Vibrio cholerae* flagellar regulatory hierarchy controls expression of virulence
664 factors. J Bacteriol 191:6555-70.
665 19. Tonner PD, Pittman AM, Gulli JG, Sharma K, Schmid AK. 2015. A regulatory hierarchy
666 controls the dynamic transcriptional response to extreme oxidative stress in archaea.
667 PLoS Genet 11:e1004912.
668 20. Yu H, Gerstein M. 2006. Genomic analysis of the hierarchical structure of regulatory
669 networks. Proc Natl Acad Sci U S A 103:14724-31.

670 21. Gao R, Stock AM. 2015. Temporal hierarchy of gene expression mediated by
671 transcription factor binding affinity and activation dynamics. MBio 6:e00686-15.
672 22. Feng L, Rutherford ST, Papenfort K, Bagert JD, van Kessel JC, Tirrell DA, Wingreen NS,
673 Bassler BL. 2015. A qrr noncoding RNA deploys four different regulatory mechanisms to
674 optimize quorum-sensing dynamics. Cell 160:228-40.
675 23. Levine E, Zhang Z, Kuhlman T, Hwa T. 2007. Quantitative characteristics of gene
676 regulation by small RNA. PLoS Biol 5:e229.
677 24. Busch A, Richter AS, Backofen R. 2008. IntaRNA: efficient prediction of bacterial sRNA
678 targets incorporating target site accessibility and seed regions. Bioinformatics 24:2849-
679 56.
680 25. Wright PR, Georg J, Mann M, Sorescu DA, Richter AS, Lott S, Kleinkauf R, Hess WR,
681 Backofen R. 2014. CopraRNA and IntaRNA: predicting small RNA targets, networks and
682 interaction domains. Nucleic Acids Res 42:W119-23.
683 26. Morita T, Kawamoto H, Mizota T, Inada T, Aiba H. 2004. Enolase in the RNA
684 degradosome plays a crucial role in the rapid decay of glucose transporter mRNA in the
685 response to phosphosugar stress in *Escherichia coli*. Mol Microbiol 54:1063-75.
686 27. Morita T, Maki K, Aiba H. 2005. RNase E-based ribonucleoprotein complexes:
687 mechanical basis of mRNA destabilization mediated by bacterial noncoding RNAs.
688 Genes Dev 19:2176-86.
689 28. Kawamoto H, Koide Y, Morita T, Aiba H. 2006. Base-pairing requirement for RNA
690 silencing by a bacterial small RNA and acceleration of duplex formation by Hfq. Mol
691 Microbiol 61:1013-22.
692 29. Fei J, Singh D, Zhang Q, Park S, Balasubramanian D, Golding I, Vanderpool CK, Ha T.
693 2015. RNA biochemistry. Determination of *in vivo* target search kinetics of regulatory
694 noncoding RNA. Science 347:1371-4.
695 30. Morita T, Mochizuki Y, Aiba H. 2006. Translational repression is sufficient for gene
696 silencing by bacterial small noncoding RNAs in the absence of mRNA destruction. Proc
697 Natl Acad Sci U S A 103:4858-63.
698 31. Moon K, Gottesman S. 2011. Competition among Hfq-binding small RNAs in *Escherichia*
699 *coli*. Mol Microbiol 82:1545-62.
700 32. Santiago-Frangos A, Kavita K, Schu DJ, Gottesman S, Woodson SA. 2016. C-terminal
701 domain of the RNA chaperone Hfq drives sRNA competition and release of target RNA.
702 Proc Natl Acad Sci U S A 113:E6089-E6096.
703 33. Schu DJ, Zhang A, Gottesman S, Storz G. 2015. Alternative Hfq-sRNA interaction
704 modes dictate alternative mRNA recognition. EMBO J 34:2557-73.
705 34. Sun Y, Vanderpool CK. 2011. Regulation and function of *Escherichia coli* sugar efflux
706 transporter A (SetA) during glucose-phosphate stress. J Bacteriol 193:143-53.
707 35. Miller JH. 1972. Experiments in bacterial genetics. Cold Spring Harbor Laboratory Press,
708 Cold Spring Harbor, NY.
709 36. Datsenko KA, Wanner BL. 2000. One-step inactivation of chromosomal genes in
710 *Escherichia coli* K-12 using PCR products. Proc Natl Acad Sci U S A 97:6640-5.
711 37. Yu D, Ellis HM, Lee EC, Jenkins NA, Copeland NG, Court DL. 2000. An efficient
712 recombination system for chromosome engineering in *Escherichia coli*. Proc Natl Acad
713 Sci U S A 97:5978-83.
714 38. Corcoran CP, Podkaminski D, Papenfort K, Urban JH, Hinton JC, Vogel J. 2012.
715 Superfolder GFP reporters validate diverse new mRNA targets of the classic porin
716 regulator, MicF RNA. Mol Microbiol 84:428-45.
717 39. Morita T, Maki K, Aiba H. 2012. Detection of sRNA-mRNA interactions by electrophoretic
718 mobility shift assay. Methods Mol Biol 905:235-44.

719 40. Wilkinson KA, Merino EJ, Weeks KM. 2006. Selective 2'-hydroxyl acylation analyzed by
720 primer extension (SHAPE): quantitative RNA structure analysis at single nucleotide
721 resolution. Nat Protoc 1:1610-6.
722 41. Mortimer SA, Weeks KM. 2009. Time-resolved RNA SHAPE chemistry: quantitative
723 RNA structure analysis in one-second snapshots and at single-nucleotide resolution. Nat
724 Protoc 4:1413-21.
725 42. Karabiber F, McGinnis JL, Favorov OV, Weeks KM. 2013. QuShape: rapid, accurate,
726 and best-practices quantification of nucleic acid probing information, resolved by
727 capillary electrophoresis. RNA 19:63-73.
728 43. McGinnis JL, Duncan CD, Weeks KM. 2009. High-throughput SHAPE and hydroxyl
729 radical analysis of RNA structure and ribonucleoprotein assembly. Methods Enzymol
730 468:67-89.
731 44. So LH, Ghosh A, Zong C, Sepulveda LA, Segev R, Golding I. 2011. General properties
732 of transcriptional time series in *Escherichia coli*. Nat Genet 43:554-60.
733 45. Rust MJ, Bates M, Zhuang X. 2006. Sub-diffraction-limit imaging by stochastic optical
734 reconstruction microscopy (STORM). Nat Methods 3:793-5.
735 46. Huang B, Wang W, Bates M, Zhuang X. 2008. Three-dimensional super-resolution
736 imaging by stochastic optical reconstruction microscopy. Science 319:810-3.
737 47. Lorenz R, Luntzer D, Hofacker IL, Stadler PF, Wolfinger MT. 2016. SHAPE directed
738 RNA folding. Bioinformatics 32:145-7.
739 48. Ishikawa H, Otaka H, Maki K, Morita T, Aiba H. 2012. The functional Hfq-binding module
740 of bacterial sRNAs consists of a double or single hairpin preceded by a U-rich sequence
741 and followed by a 3' poly(U) tail. RNA 18:1062-74.
742

743 **FIGURE LEGENDS**

744 **Figure 1. Model for SgrS target prioritization during glucose-phosphate stress.**

745 Glucose or the analogs αMG and 2-deoxyglucose are phosphorylated during transport
746 through the phosphotransferase system proteins $EIICB^{Glc}$ (PtsG) or $EIICD^{Man}$ (ManYZ).
747 If sugar-phosphates are not metabolized, the glucose-phosphate stress response is
748 triggered, and the transcription factor SgrR becomes active and promotes *sgrS*
749 transcription. The RNA chaperone Hfq promotes SgrS-mediated translational repression
750 of *ptsG* and *manXYZ* mRNAs, reducing synthesis of sugar transporters. SgrS stabilizes
751 *yigL* mRNA, promoting sugar phosphatase (YigL) synthesis. SgrS-mediated repression
752 of *asd, purR, folE* and *adiY* likely reroutes metabolism to restore homeostasis during
753 stress recovery. The hypothetical sequence of regulatory events following stress
754 induction is represented from left to right as SgrS levels increase over time. When SgrS

755 concentrations are low, only the highest priority targets are regulated. When stress
756 persists and concentrations of SgrS increase, lower priority targets are regulated.
757 **Figure 2. Efficiency of target regulation by SgrS.** A) Representation of genetic
758 constructs in two compatible plasmids used to study target regulation by SgrS. One
759 plasmid contains full-length SgrS under the control of the aTc-inducible P_{Tet} promoter.
760 A second plasmid contains a P_{Lac} promoter and the relevant region encoding each SgrS
761 target (including the SgrS binding site) translationally fused to a superfolder *gfp* reporter
762 gene. B-F) Regulated activity was plotted as a function of basal activity (see text for
763 description) for (B) *ptsG*, (C) *manX*, (D) *purR,* (E) *asdI,* and (F) *yigL* fused to *sfgfp*
764 reporter gene. Without SgrS-mediated regulation, we obtained a line with a slope =1.
765 The plots with slopes <1 indicate repression of (B) *ptsG*, (C) *manX*, (D) *purR* and (E)
766 *asdI* by SgrS. The plot with a slope of >1 is indicative of activation of (F) *yigL*.
767 **Figure 3. Regulatory hierarchy established by SgrS.** Regulated activity was plotted
768 as a function of basal activity for *ptsG*, *manX*, *purR, asdI,* and *yigL* fusions. Lack of
769 SgrS regulation is indicated by a line with a slope =1. The plots with slopes <1 indicate
770 repression (*ptsG*, *manX*, *purR* and *asdI*) by SgrS. The plot with slope >1 indicates
771 activation (*yigL*). Target fusion activity was monitored at different levels of SgrS
772 induction by aTc: (A) 10 ng/ml, (B) 20 ng/ml, (C) 30 ng/ml, (D) 40 ng/ml, (E) 50 ng/ml.
773 **Figure 4. SgrS binding to target mRNAs *in vitro***. A) SgrS was labeled with ^{32}P and
774 incubated with unlabeled target transcripts at final concentrations of 0 μM - 16 μM .
775 Electrophoretic mobility shift assays (EMSAs) were performed after incubating full-
776 length SgrS (+1 to +227) with its target transcripts (A) *ptsG* (+1 to +240), *manX* (+1 to
777 +240), *purR* (+1 to +230), *yigL* (-191 to +50 relative to ATG translation start of *yigL*),

778 *asdI* (+1 to +110), and *asdII* (+71 to +310). B-D) Target transcripts (B) *ptsG* (+1 to
779 +240), (C) *manX* (+1 to +240), (D) *asdI* (+1 to +110) were labeled with ^{32}P and
780 incubated with unlabeled SgrS. EMSAs were performed to resolve complex formation.
781 Band densities were measured for replicate experiments (n, top left) and plotted to
782 determine dissociation constant (K_D, bottom right) values for (B) *ptsG*, (C) *manX*, and
783 (D) *asdI*. E) EMSA of radiolabeled SgrS in the presence of increasing concentrations of
784 *asdI-II* transcript. Shift in mobility corresponding to one or two SgrS bound to *asdI-II* is
785 denoted as Site I-SgrS* and Sites I-II-SgrS* respectively. F) Quantification of SgrS
786 binding with radiolabeled *asdI-II* (+1 to +240), as described above.
787 **Figure 5. Secondary structure of 5' end of *asd*.** A) Diagram showing base-pairing
788 interactions of SgrS with binding sites I and II of *asd* mRNA. B) Energy of interaction
789 predicted by IntaRNA (26). "Structured" indicates pairing between full length SgrS (+1 to
790 +227) and *asdI-II* (+1 to +180). Plotted is the energy of interactions at either site I (*asdI*)
791 or site II (*asdII*). "Isolated" indicates interactions between isolated binding sites: SgrS
792 (+158 to +176) with *asdI* (+31 to +49) and SgrS (+158 to +178) pairing with *asdII* (+110
793 to +129). C) The structure of the *asdI-II* RNA alone or in complex with SgrS was probed
794 with NMIA and the modified RNA was analyzed by primer extension inhibition. SHAPE
795 reactivity (difference between the frequency of primer extension products at each
796 nucleotide in +NMIA vs. -NMIA samples) was then used as a parameter in the Vienna
797 RNAprobing WebServer (47) to predict the secondary structure of the *asdI-II* RNA.
798 Colors indicate SHAPE reactivity as follows: red, highly reactive (≥ 0.8); gold, reactive
799 (0.4-0.79); green, moderately reactive (0.2-0.39); blue, minimally reactive (0.1-0.19);
800 grey, unreactive (< 0.01). Distinct structures were observed in the absence of SgrS and

801 in the presence of saturating concentrations of SgrS. The SHAPE reactivity of *asdI-II*
802 RNA alone (left) or in the presence of 5-fold excess SgrS (right) is mapped to the
803 predicted secondary structures. (D) SHAPE reactivity as a function of SgrS
804 concentration for each binding site (top, site I; bottom, site II). Only nucleotides with a
805 significant (≥ 0.1) change in reactivity are shown. Error bars denote SEM, n = 9. (E)
806 Relative SHAPE reactivity (difference in the SHAPE reactivity in the presence of SgrS
807 vs. the absence of SgrS) of the *asdI-II* RNA in the presence of wild-type (top) or mutant
808 (bottom) SgrS. Error bars denote SEM, n = 9 (WT), 6 (MT). The *asdI-II* RNA
809 nucleotides are numbered below the X-axis and the SgrS binding sites are indicated.
810 **Figure 6. STORM imaging of SgrS regulation of *asd* variants.** A) Illustration of *asdI-*
811 *II*, *asdI* and *asdII* translationally fused to *lacZ* reporter with SgrS binding sites I and II
812 marked. B-D) 2D projection of 3D super-resolution images of SgrS and *lacZ* mRNA for
813 the different *asd-lacZ* variants, labeled by smFISH, before and after 10 min induction
814 with 1% αMG. (B), (C) and (D) correspond to *asdI-lacZ*, *asdII-lacZ,* and *asdI-II-*
815 *lacZ* shown in (A). Probability distributions of RNA copy numbers in individual cells for
816 30-250 cells are plotted next to the representative images.
817 **Figure 7. SgrS binding cooperativity allows for improved repression of *asd***
818 **translation.** A) Illustration of *asdI* and *asdI-II* constructs with SgrS binding sites marked.
819 Graphs show comparison of SgrS regulation of *asdI* and *asdI-II* variants in (B) wild-type
820 and (D) *rne701* mutant by plotting regulated activity over basal activity at various SgrS
821 expression levels (20-100 ng/ml aTc). Regulatory hierarchy of SgrS targets in (C) wild-
822 type and (E) *rne701* mutant strains. Regulation of target genes at one SgrS expression

823 level (40 ng/ml aTc) are compared by plotting regulated activity over basal activity of the

824 *gfp* reporter.

825 **Figure 8. SgrS regulation of transcriptional *asd-lacZ* fusions.** β-galactosidase

826 activity of (A) *asdI-lacZ* (+1 to +64) and *asdI-II-lacZ* (+1 to +277) was (B) assayed in

827 response to SgrS expression from a plasmid (and vector control) in WT and *rne701*

828 background strains.

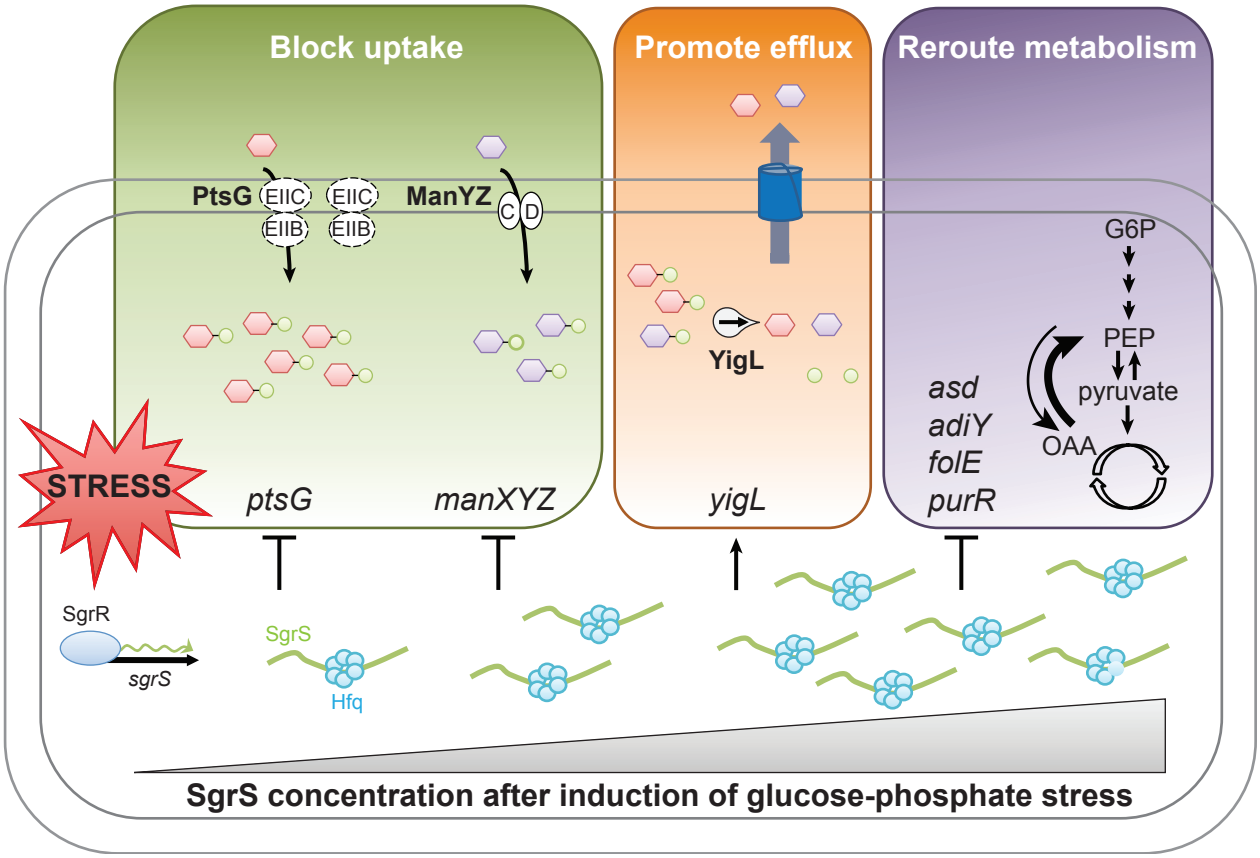

Figure 1. Model for SgrS target prioritization during glucose-phosphate stress. Glucose or the analogs αMG and 2-deoxyglucose are phosphorylated during transport through the phosphotransferase system proteins EIICB^{Glc} (PtsG) or EIICD^{Man} (ManYZ). If sugar-phosphates are not metabolized, the glucose-phosphate stress response is triggered, and the transcription factor SgrR becomes active and promotes *sgrS* transcription. The RNA chaperone Hfq promotes SgrS-mediated translational repression of *ptsG* and *manXYZ* mRNAs, reducing synthesis of sugar transporters. SgrS stabilizes *yigL* mRNA, promoting sugar phosphatase (YigL) synthesis. SgrS-mediated repression of *asd, purR, folE* and *adiY* likely reroutes metabolism to restore homeostasis during stress recovery. The hypothetical sequence of regulatory events following stress induction is represented from left to right as SgrS levels increase over time. When SgrS concentrations are low, only the highest priority targets are regulated. When stress persists and concentrations of SgrS increase, lower priority targets are regulated.

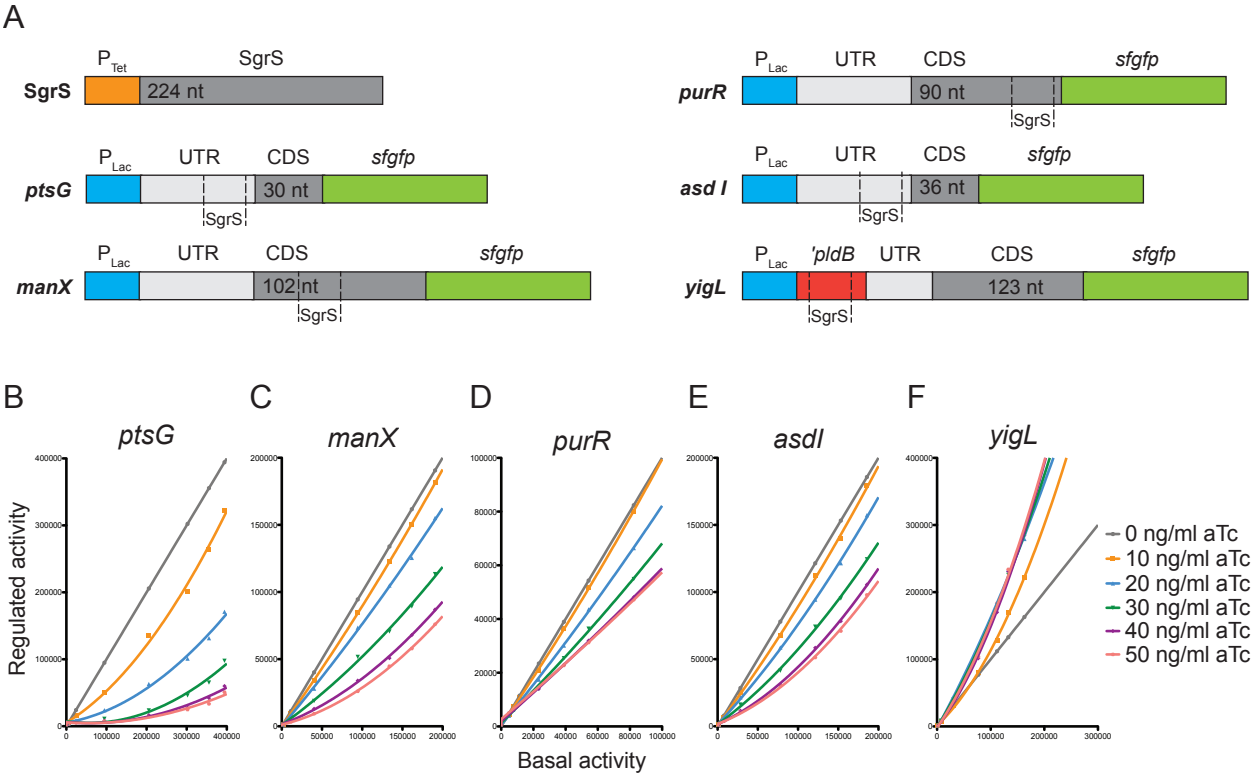

Figure 2. Efficiency of target regulation by SgrS. A) Representation of genetic constructs in two compatible plasmids used to study target regulation by SgrS. One plasmid contains full-length SgrS under the control of the aTc-inducible P_{Tet} promoter. A second plasmid contains a P_{Lac} promoter and the relevant region encoding each SgrS target (including the SgrS binding site) translationally fused to a superfolder *gfp* reporter gene. B-F) Regulated activity was plotted as a function of basal activity (see text for description) for (B) *ptsG*, (C) *manX*, (D) *purR,* (E) *asdI,* and (F) *yigL* fused to *sfgfp* reporter gene. Without SgrS-mediated regulation, we obtained a line with a slope =1. The plots with slopes <1 indicate repression of (B) *ptsG*, (C) *manX*, (D) *purR* and (E) *asdI* by SgrS. The plot with a slope of >1 is indicative of activation of (F) *yigL*.

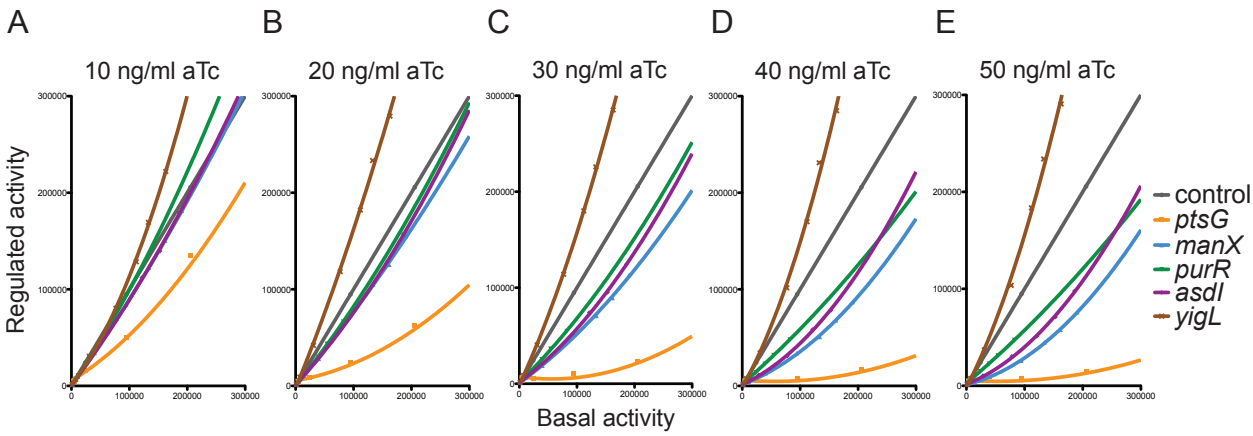

Figure 3. Regulatory hierarchy established by SgrS. Regulated activity was plotted as a function of basal activity for *ptsG*, *manX*, *purR, asdI,* and *yigL* fusions. Lack of SgrS regulation is indicated by a line with a slope =1. The plots with slopes <1, indicate repression (*ptsG*, *manX*, *purR* and *asdI*) by SgrS. The plot with slope >1 indicates activation (*yigL*). Target fusion activity was monitored at different levels of SgrS induction by aTc: (A) 10 ng/ml, (B) 20 ng/ml, (C) 30 ng/ml, (D) 40 ng/ml, (E) 50 ng/ml.

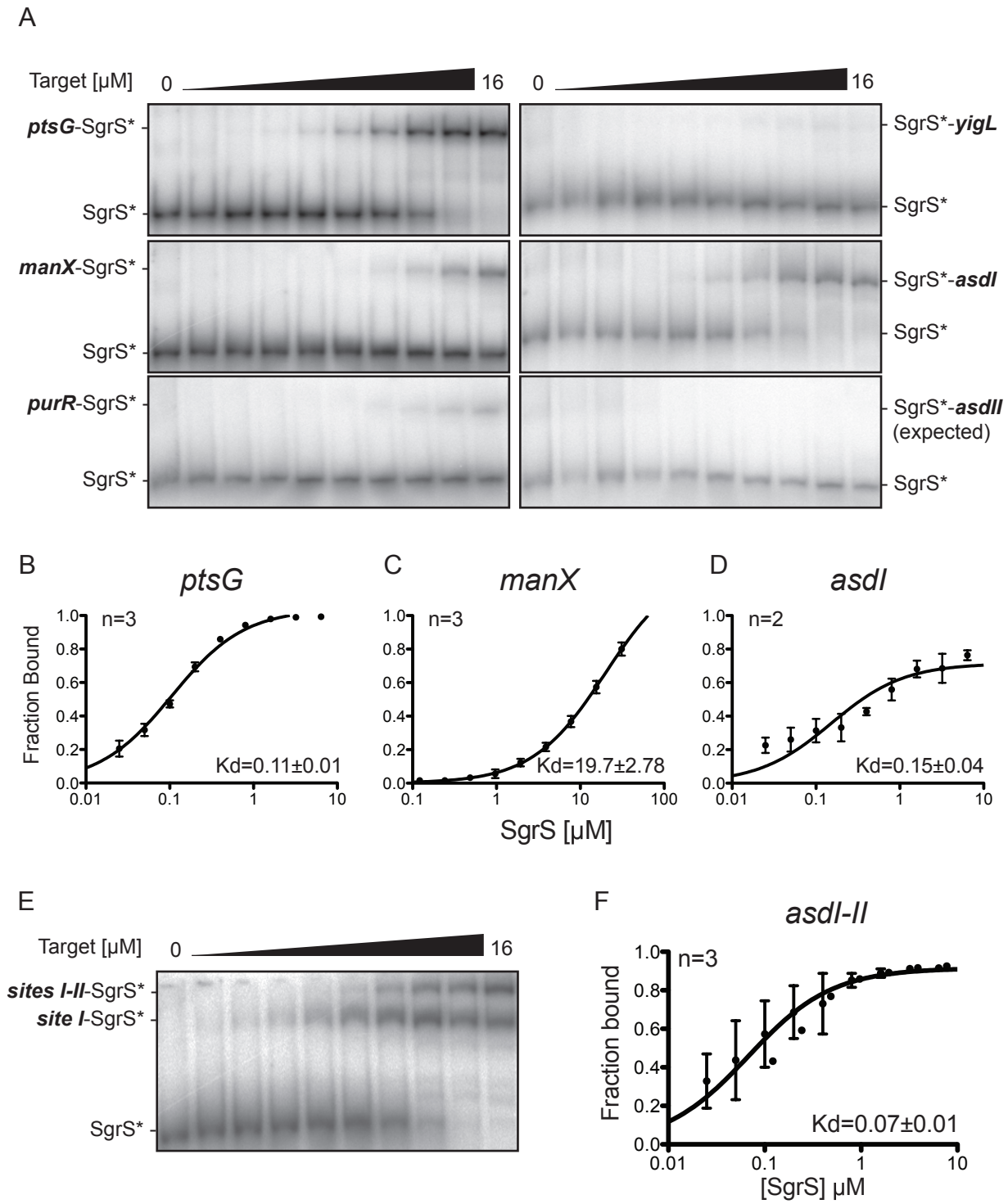

Figure 4 legend on the next page

Figure 4. SgrS binding to target mRNAs *in vitro*. A) SgrS was labeled with ^{32}P and incubated with unlabeled target transcripts at final concentrations of 0 μM - 16 μM . Electrophoretic mobility shift assays (EMSAs) were performed after incubating full-length SgrS (+1 to +227) with its target transcripts (A) *ptsG* (+1 to +240), *manX* (+1 to +240), *purR* (+1 to +230), *yigL* (-191 to +50 relative to ATG translation start of *yigL*), *asdI* (+1 to +110), and *asdII* (+71 to +310). B-D) Target transcripts (B) *ptsG* (+1 to +240), (C) *manX* (+1 to +240), (D) *asdI* (+1 to +110) were labeled with ^{32}P and incubated with unlabeled SgrS. EMSAs were performed to resolve complex formation. Band densities were measured for replicate experiments (n, top left) and plotted to determine dissociation constant (K_D, bottom right) values for (B) *ptsG*, (C) *manX*, and (D) *asdI*. E) EMSA of radiolabeled SgrS in the presence of increasing concentrations of *asdI-II* transcript. Shift in mobility corresponding to one or two SgrS bound to *asdI-II* is denoted as Site I-SgrS* and Sites I-II-SgrS* respectively. F) Quantification of SgrS binding with radiolabeled *asdI-II* (+1 to +240), as described above.

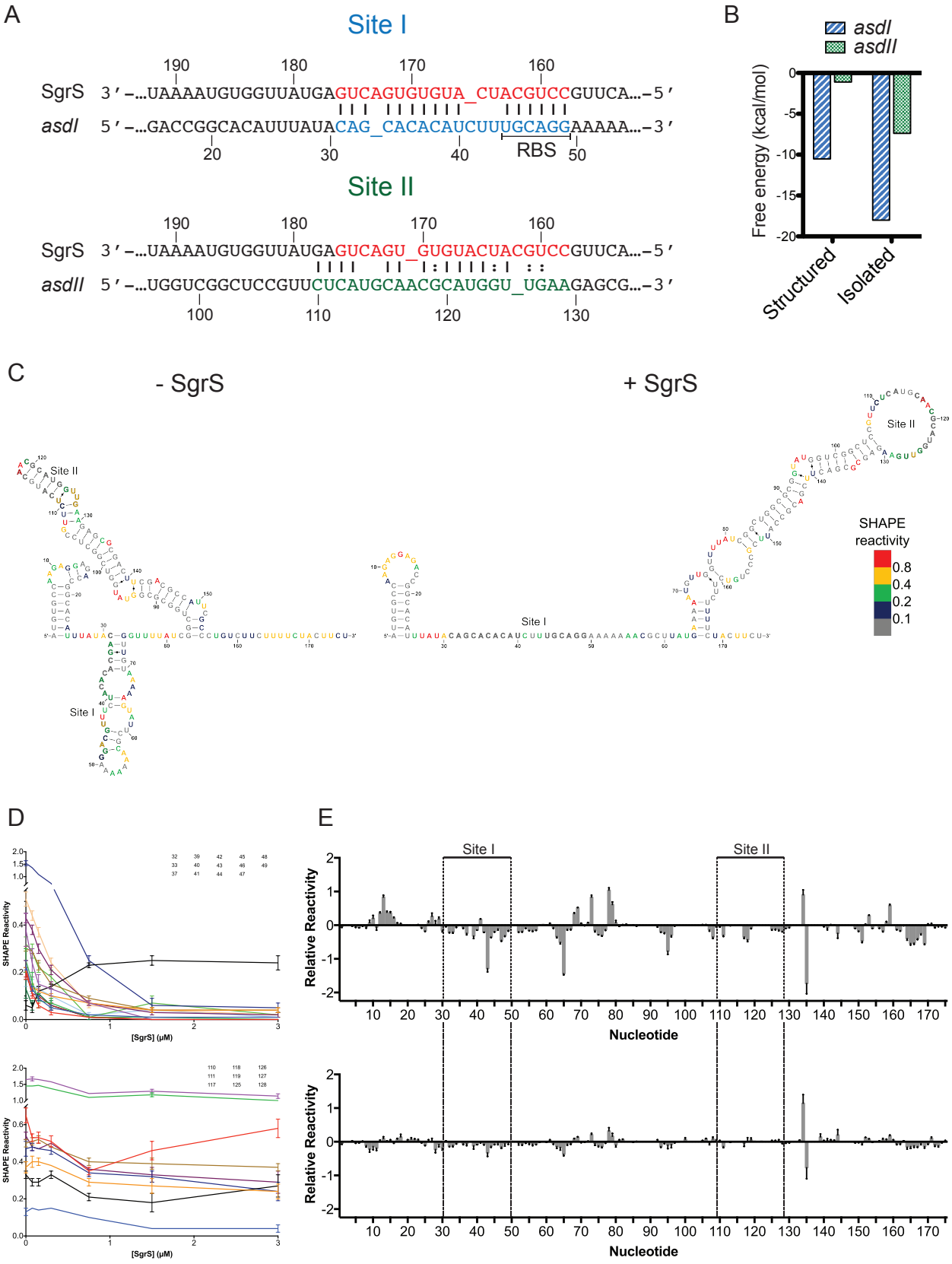

Figure 5 legend on the next page

Figure 5. Secondary structure of 5' end of *asd*. A) Diagram showing base-pairing interactions of SgrS with binding sites I and II of *asd* mRNA. B) Energy of interaction predicted by IntaRNA (26). "Structured" indicates pairing between full length SgrS (+1 to +227) and *asdI-II* (+1 to +180). Plotted is the energy of interactions at either site I (*asdI*) or site II (*asdII*). "Isolated" indicates interactions between isolated binding sites: SgrS (+158 to +176) with *asdI* (+31 to +49) and SgrS (+158 to +178) pairing with *asdII* (+110 to +129). C) The structure of the *asdI-II* RNA alone or in complex with SgrS was probed with NMIA and the modified RNA was analyzed by primer extension inhibition. SHAPE reactivity (difference between the frequency of primer extension products at each nucleotide in +NMIA vs. -NMIA samples) was then used as a parameter in the Vienna RNAprobing WebServer (55) to predict the secondary structure of the *asdI-II* RNA. Colors indicate SHAPE reactivity as following: red, highly reactive (≥ 0.8); gold, reactive (0.4-0.79); green, moderately reactive (0.2-0.39); blue, minimally reactive (0.1-0.19); grey, unreactive (< 0.01). Distinct structures were observed in the absence of SgrS and in the presence of saturating concentrations of SgrS. The SHAPE reactivity of *asdI-II* RNA alone (left) or in the presence of 5-fold excess SgrS (right) is mapped to the predicted secondary structures. (D) SHAPE reactivity as a function of SgrS concentration for each binding site (top, site I; bottom, site II). Only nucleotides with a significant (≥ 0.1) change in reactivity are shown. Error bars denote SEM, n = 9. (E) Relative SHAPE reactivity (difference in the SHAPE reactivity in the presence of SgrS vs. the absence of SgrS) of the *asdI-II* RNA in the presence of wild-type (top) or mutant (bottom) SgrS. Error bars denote SEM, n = 9 (WT), 6 (MT). The *asdI-II* RNA nucleotides are numbered below the X-axis and the SgrS binding sites are indicated.

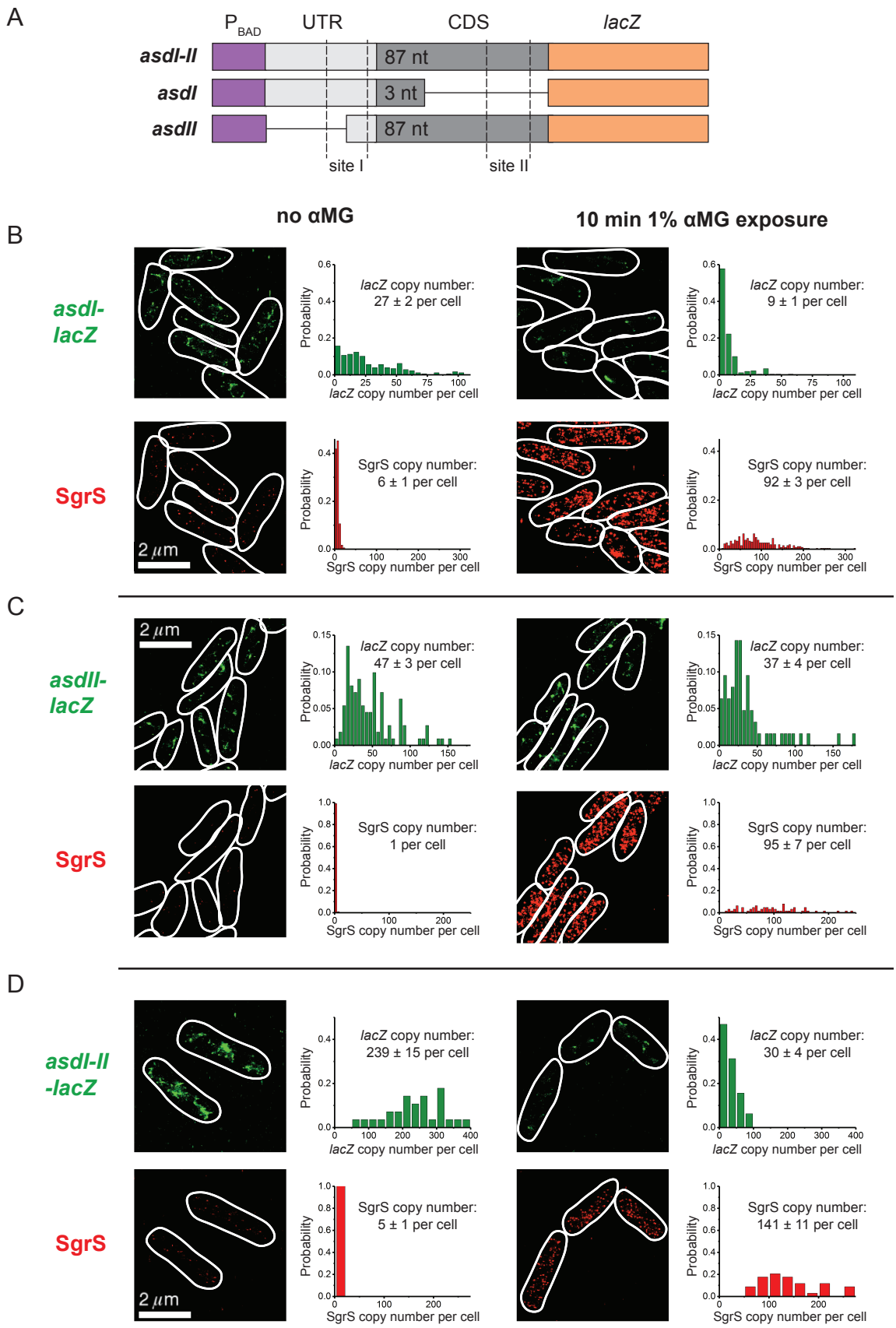

Figure 6 legend on the next page

Figure 6. STORM imaging of SgrS regulation of *asd* variants. A) Illustration of *asdI-II*, *asdI* and *asdII* translationally fused to *lacZ* reporter with SgrS binding sites I and II marked. B-D) 2D projection of 3D super-resolution images of SgrS and *lacZ* mRNA for the different *asd-lacZ* variants, labeled by smFISH, before and after 10 min induction with 1% αMG. (B), (C) and (D) correspond to *asdI-lacZ*, *asdII-lacZ,* and *asdI-II-lacZ* shown in (A). Probability distributions of RNA copy numbers in individual cells for 30-250 cells are plotted next to the representative images.

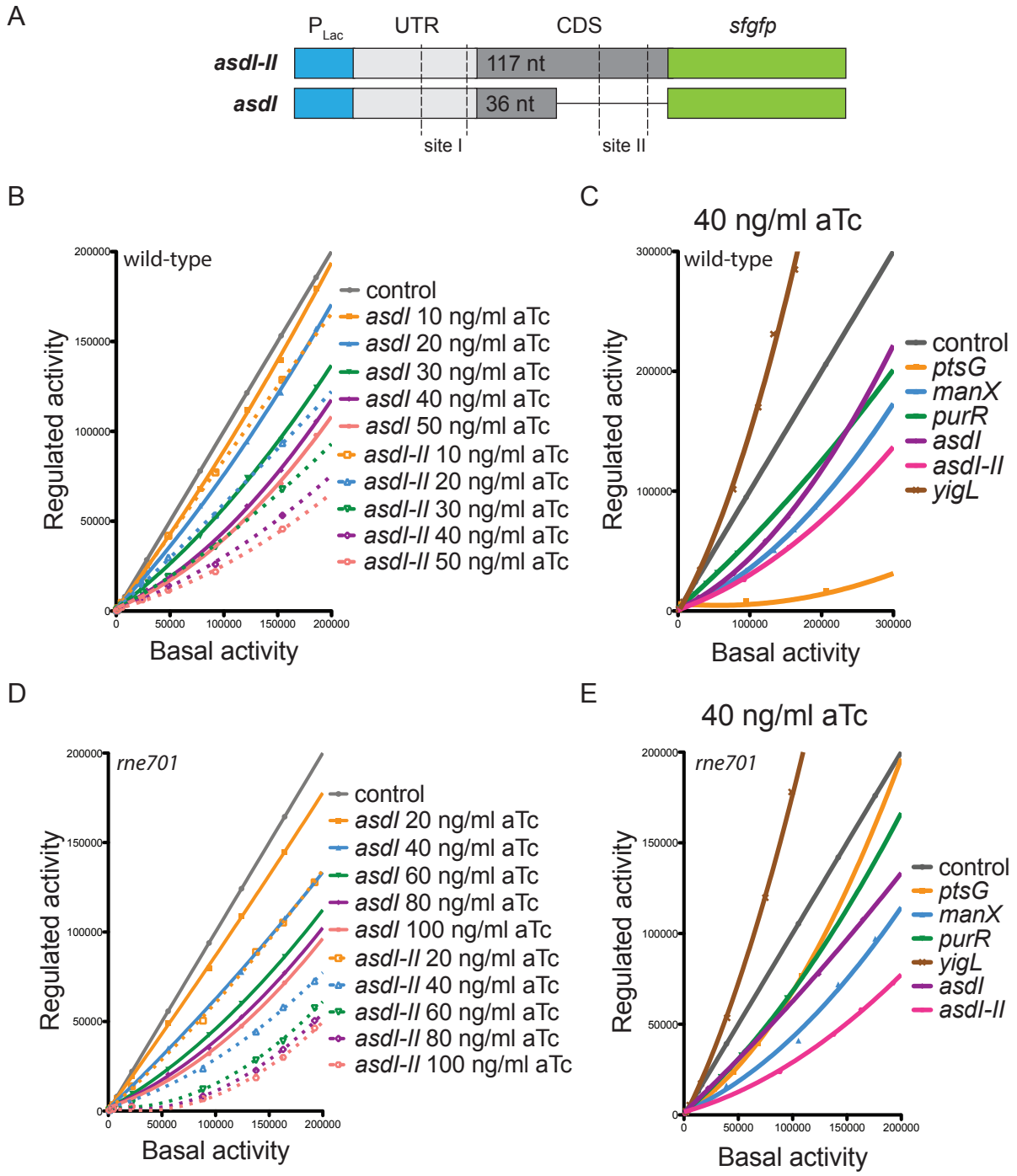

Figure 7. SgrS binding cooperativity allows for improved repression of *asd* translation. A) Illustration of *asdI* and *asdI-II* constructs with SgrS binding sites marked. Graphs show comparison of SgrS regulation of *asdI* and *asdI-II* variants in (B) wild-type and (D) *rne701* mutant by plotting regulated activity over basal activity at various SgrS expression levels (20-100 ng/ml aTc). Regulatory hierarchy of SgrS targets in (C) wild-type and (E) *rne701* mutant strains. Regulation of target genes at one SgrS expression level (40 ng/ml aTc) are compared by plotting regulated activity over basal activity of the *gfp* reporter.

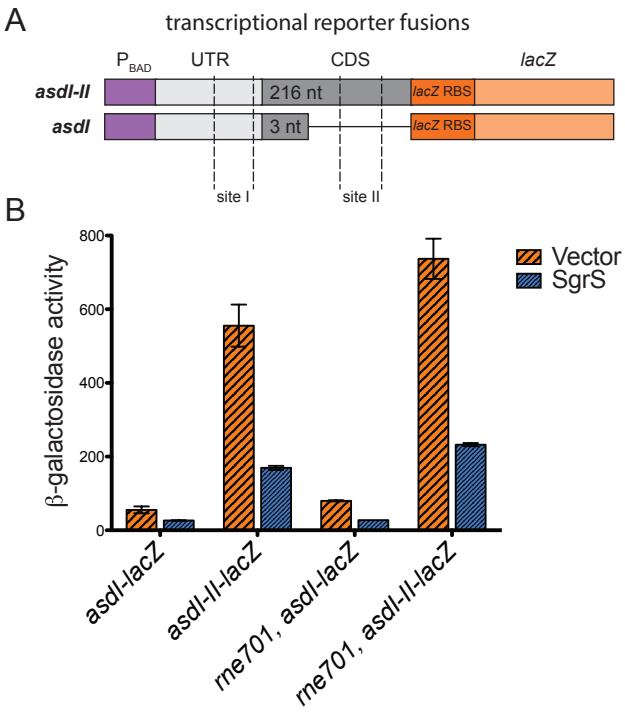

Figure 8. SgrS regulation of transcriptional *asd-lacZ* fusions. β-galactosidase activity of (A) *asdI-lacZ* (+1 to +64) and *asdI-II-lacZ* (+1 to +277) was (B) assayed in response to SgrS expression from a plasmid (and vector control) in WT and *rne701* background strains.